Numerical simulation of physical instabilities in a lined channel using the linearized Euler Equations

D. Marx
Institut Pprime, Site ENSIP bât. B17, 6, rue Marcel Doré, 86022 Poitiers, France
david.marx@univ-poitiers.fr

The propagation of acoustic modes in lined waveguides may be computed numerically. When the mesh is fine enough, it is current to observe instabilities whose numerical or physical character is difficult to assess. The matter is even more complicated when the ill-posed Myers boundary condition is used. In this work the 2D linearized Euler equations are solved in the time domain in order to calculate the propagation of an acoustic mode in a channel with a rigid top wall and a lined bottom wall. The mean flow is highly sheared at the wall where it satisfies a no-slip condition so that the Myers impedance boundary condition is avoided. The liner is modeled using a mass-spring-damper law with a known impedance. This type of liner is often unstable, and a physical instability (surface wave) is observed when the mesh is refined. The eigenfunction shape and growth rate are compared with that obtained by solving an eigenvalue problem (linear stability analysis). The role of the numerical selective filtering in removing the spuriously unstable continuous spectrum is also discussed. An example of rigid/lined/rigid wall is also shown, where the instability is converted into an acoustic mode of large amplitude at the lined/rigid transition.

1 Introduction

Noise reduction from aeroengines crucially relies on acoustic linings. These are found in the presence of strong shear flows and numerical simulations are appealing to compute sound propagation in this case. For several types of problems (transient, broadband, nonlinear) it is desirable to perform the simulation of lined ducts in the time domain and many recent works have been devoted to time-domain solvers with appropriate liner boundary conditions [1].

Liners are characterized by their impedance, a quantity belonging to the frequency domain. However, several techniques make it possible to use a time-domain impedance boundary condition (TDIBC). For a mass-spring-damper (MSD) liner, a simple time-domain implementation is possible and has been presented by Tam and Auriault [2].

Generally, the presence of the shear flow is an issue. So as not to describe the details of the boundary layer, one may introduce a slip velocity at the lined wall of the duct, and this is usually dealt with by using Myers' boundary condition. By using this boundary condition, Li *et al.* [3] found an agreement between their numerical predictions and the benchmark data of Jones *et al.* [4]. Another possibility is to suppose that there is a no-slip mean flow at the wall and to use the regular no-flow boundary condition. This was done for example in [5] and [6]. Using a parabolic flow, these studies show a good agreement with the measurement in [4].

Another issue is the stability of the TDIBC, and this is mainly connected to flow. Tam and Auriault [2] note that their boundary condition is unstable with a plug flow. Ozyoruk and Long [7] computations also suffer from stability problems when using Myers' boundary condition with a plug flow. However, their computations based on a parabolic velocity profile vanishing at the wall are stable[5]. In this particular example, it is difficult to know which result is actually correct. One one hand, Myers' boundary condition is ill-posed [8, 9], meaning that very short wavelengths can be arbitrarily amplified in time, and it may spuriously turn a stable flow into an unstable one. On the other hand, the parabolic velocity profile is not as sheared as the original experimental turbulent velocity profile, and as a result its use may render stable an actually unstable flow.

The objective of the present paper is to answer the question as to whether it is possible to simulate a physical instability using the linearized Euler equations (LEE) in the time-domain and to provide a reference unstable configuration. Instabilities above linings are usually surface waves which require a refined grid close to the wall in order to be correctly described. To discard any instability possibly associated with the Myers boundary condition when using small grid sizes, Myers' boundary condition is avoided. The mean flow thus vanishes at the wall. The impedance model is kept simple as it consists of a MSD model [2] that can be implemented easily in a time-domain solver. One way to be sure of the physical nature of the instability observed in the LEE is to compare it with the modes calculated by solving a linear eigenvalue problem (EVP). In the following the model for the LEE is presented first. The modal equivalent and the resulting EVP are presented next. A cross-validation of the LEE solver and the EVP solver is done in a simple case where the flow is not highly sheared. Finally results for a velocity profile that has a large shear at the walls are presented.

2 Problem formulation

The equations describing the problem are the LEE :

$$\frac{\partial \rho'}{\partial t} + U_0 \frac{\partial \rho'}{\partial x} + \left(\frac{\partial u'}{\partial x} + \frac{\partial v'}{\partial y} \right) = -s(x)(\rho' - \rho_t) \quad (1)$$

$$\frac{\partial u'}{\partial t} + U_0 \frac{\partial u'}{\partial x} + v' \frac{dU_0}{dy} + \frac{\partial p'}{\partial x} = -\sigma u' - s(x)(u' - u_t) \quad (2)$$

$$\frac{\partial v'}{\partial t} + U_0 \frac{\partial v'}{\partial x} + \frac{\partial p'}{\partial y} = -\sigma v' - s(x)(v' - v_t) \quad (3)$$

$$\frac{\partial p'}{\partial t} + U_0 \frac{\partial p'}{\partial x} + \left(\frac{\partial u'}{\partial x} + \frac{\partial v'}{\partial y} \right) = -s(x)(p' - p_t) \quad (4)$$

The terms with σ are additional friction terms, while the terms with $s(x)$ are sponge layer terms used in the numerical simulation to introduce a wave into the domain or to obtain a non reflecting boundary condition, as in [10]. The subscript t indicates target values. The boundary condition at the top rigid wall is :

$$v'(1) = 0 \quad (5)$$

The liner at the bottom wall is taken to be of the MSD type. The pressure and the normal velocity are then related by the following equation [2] :

$$M \frac{\partial^2 v'}{\partial t^2} + R \frac{\partial v'}{\partial t} + K v' = -\frac{\partial p'}{\partial t} \qquad (y = -1) \quad (6)$$

Equations (2-6) are discretized in space and time and solved using a 4th order Runge Kutta method for time integration and the DRP scheme for the spatial derivatives. A selective filter is used to damp out high wavelength oscillations [11]. For the lined surface, a method comparable to that in Tam and Auriault [2] is used. Equation (6) is split into two first order equations according to :

$$\frac{\partial v'}{\partial t} = Q' \quad (7)$$

$$\frac{\partial Q'}{\partial t} = \frac{1}{M}\left[-\frac{\partial p'}{\partial t} - RQ' - Kv'\right] \quad (8)$$

where Q' is an auxiliary variable that is advanced in time with the Runge-Kutta scheme. Contrary to what is done in [2], no pressure ghost point is used : at the lined wall at y=-1, the boundary condition in Eq. (7) is simply used *in place of* the governing equation for the transverse velocity, Eq. (3).

3 Eigenvalue problem

To obtain the modal solutions to Euler Eqs. (1-4), every fluctuating quantity is written as $u'(x,y,t) = \hat{u}(y)e^{i(\alpha x-\omega t)}$, where α is the non-dimensional wavenumber, ω is the non-dimensional angular frequency, and $\hat{u}$ is a complex eigenfunction. Injecting this decomposition into Eqs. (1-4), one obtains (here, the sponge layer term is ignored, $s(x)$=0, since it is used only for the numerical simulation of the LEE) :

$$\mathrm{i}(\alpha U_0 - (\omega + \mathrm{i}\sigma))\hat{u} + \hat{v}\frac{\mathrm{d}U_0}{\mathrm{d}y} + \mathrm{i}\alpha\hat{p} = F_y(\hat{u}) \quad (9)$$

$$\mathrm{i}(\alpha U_0 - (\omega + \mathrm{i}\sigma))\hat{v} + \frac{\mathrm{d}\hat{p}}{\mathrm{d}y} = F_y(\hat{v}) \quad (10)$$

$$\mathrm{i}(\alpha U_0 - \omega)\hat{p} + \left(\mathrm{i}\alpha\hat{u} + \frac{\mathrm{d}\hat{v}}{\mathrm{d}y}\right) = F_y(\hat{p}) \quad (11)$$

and $\hat{\rho}$=$\hat{p}$ from Eqs. (1) and (4). In these equations a further term $F_y()$ has been introduced. It represents a filter in the y-direction. It may be seen as a high order differential operator involving y-derivatives. When the equations are discretized, this filter is replaced by the same discrete selective filter that is used in the LEE numerical solver, so that the effect of selective filtering is taken into account in the EVP. The filter in the x-direction is not taken into account, assuming that the discretization in the x-direction is sufficiently good. In the y direction however, the eigenfunction can have sharp variations, and it is justified to take into account the effect of the filter in that direction. The boundary conditions (5) and (6) become :

$$\hat{v}(1) = 0 \quad (12)$$

$$\frac{\hat{p}(-1)}{\hat{v}(-1)} = -Z(\omega) \text{ with } Z(\omega) = R - \mathrm{i}\left(M\omega - \frac{K}{\omega}\right) \quad (13)$$

Equation (13) is a classical impedance condition (the minus sign is due to the normal vector being directed inward). Equations (9-11) together with boundary conditions (12-13) form an EVP. This can be solved by discretizing the equations and solving the resulting matrix EVP [12]. In [12] the differentiation matrix is based on a Chebyshev collocation scheme but it may be based on the same DRP differentiation scheme as used in the LEE solver.

4 Validation

To validate the flow solver, a monochromatic plane wave at angular frequency ω is introduced into the numerical domain at x=0, and the pressure field computed using the LEE solver is compared to a sum of modes :

$$p_{\mathrm{modal}}(x,y,t) = \sum_{j=1}^{N_{\mathrm{cuton}}} a_j\hat{p}_j(y)e^{\mathrm{i}(\alpha_j x-\omega t)} \quad (14)$$

where the modes $\hat{p}_j$ and the corresponding wavenumber α_j are obtained by solving the EVP (9-13) for the given ω. All the modes should be taken into account in the sum, but presently only the N_{cuton} cuton modes are used. The modal amplitudes, a_j, should be such that $p_{\mathrm{modal}}(x = 0,y,t) = g(y,t)$, where $g(y,t) = Ae^{-\mathrm{i}\omega t}$ is the imposed plane wave at x=0, with A a complex amplitude. Obtaining these modal amplitudes is not totally straightforward because the modes are not normal [13]. Ideally one would use the bi-orthogonality conditions provided by the adjoint eigenfunctions. To keep things simple they are presently obtained by solving the following problem in the least mean square sense, as in [13] :

$$\sum_{i=1}^{N_{\mathrm{cuton}}}\underbrace{\left(\sum_{k=1}^{N_y}\hat{p}_i(y_k)\hat{p}_j^*(y_k)\right)}_{=T_{ij}}a_i = \sum_{k=1}^{N_y}g(y_k)\hat{p}_j^*(y_k) \qquad \forall j = 1...N_{\mathrm{cuton}} \quad (15)$$

where y_k, k=1...N_y, are the collocations points, and * denotes complex conjugation. This is a linear system for the vector of modal amplitudes and is solved using a pseudo inverse of T, the matrix with elements T_{ij}.

The flow is parabolic with peak central velocity $U_0(0)$=0.5. A plane wave is injected at the inlet with ω=4π. The liner covering the bottom wall has the following characteristics : R=0.5, M=0.0625, K=5.33. In such conditions the EVP shows that the flow is stable. The grid is regular with Δx=Δy=0.033, and CFL=1. The number of points are N_x=207 and N_y=61. N_{cuton}=8 modes are used in (14). The instantaneous pressure fields obtained by solving the time LEE and the modal solution (14) are shown in Fig. 1 for an arbitrary A=1 amplitude at the inlet plane. Both solutions compare very well. One can observe energy concentration close to the top rigid wall due to the refraction by the mean flow, and energy absorption at the bottom lined wall. This allows a cross-validation of our solvers.

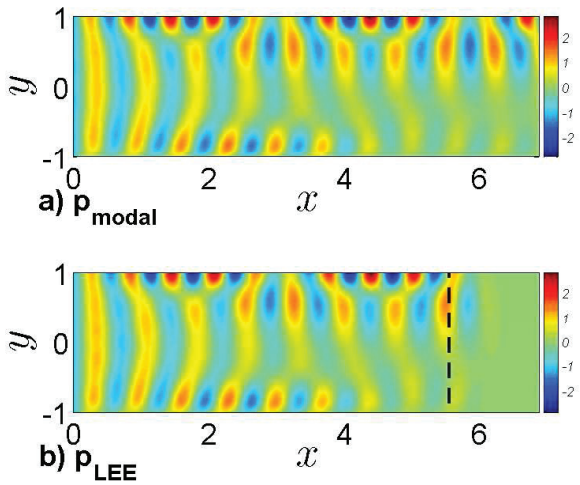

Figure 1 – Pressure field due to a plane wave at the inlet of the duct with a parabolic mean flow. Comparison between the instantaneous pressure field computed using the modal solution and the one computed using the time-domain LEE. The dashed line indicates the outlet sponge layer limit.

5 Propagation with highly shear flows

A more realistic velocity profile is considered, which is an analytical approximation for the one measured by Jones *et al.* [4] in their benchmark data at Mach number M_0=0.335. Their experimental configuration is three-dimensional and the profile in the middle section of the channel is considered for a 2D simulation, with the following analytical expression :

$$U_0(y) = (M_1 - M_2 y^2)\left(1 - e^{-(y+1)/\delta}\right)\left(1 - e^{-(1-y)/\delta}\right) \quad (16)$$

where M_1=0.4, M_2=0.124, δ=0.015. Figure 2 compares the measured profile and that given by Eq. (16). In [3] an

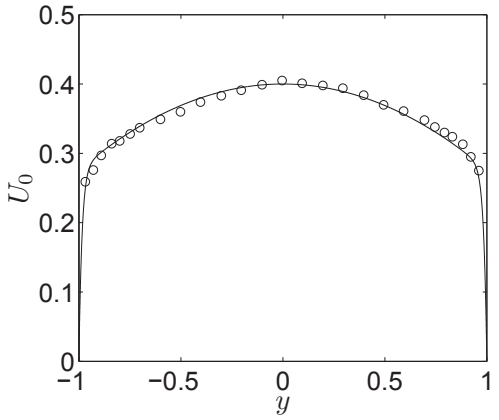

Figure 2 – Comparison between the measured profile by Jones *et al.* [4] in the middle section of their channel and the analytical expression (16) used in the present paper. Averaged Mach number : U_0=0.335.

instability is observed for the same flow at a frequency of 1 kHz (corresponding to a normalized ω ~0.4712389), and we will thus consider this frequency. The normalized impedance given by Jones et al. [4] is then Z=0.19-0.15i (given here for the present time convention). For the MSD model, the reactance needs to be distributed between the mass and the spring constant : we take in the following M ~1.669248 and K=0.3, with $(M\omega - K/\omega)$ ~ 0.15. For the original resistance, R=0.19, a stability analysis shows that the modes are fastly oscillating (large α_r) and the resolution necessary to compute these modes would require two much computational effort. Hence, the resistance value is increased and the value R=1.2 or R=4 is used in the following.

5.1 Stability analysis

A wavenumber spectrum for R=1.2 and ω=0.47 is shown in Fig. 3. An unstable surface mode can be seen (checked using a Briggs-Bers criterion) with α_i <0. By tracking this mode when varying the frequency, the curve $\alpha(\omega_r)$ can be obtained and the imaginary part (the opposite of the growth rate) is shown in Fig. 4. It evidences a resonance frequency at ω ~0.47 corresponding to a maximal growth rate. For a resistance R=4 the resonance frequency is decreased to ω_r ~0.15 and the growth rate is smaller. It is important to note that the EVP, when integrated along the real line y$\in$ $(-1, 1)$ would fail to capture the surface mode when it becomes stable. To follow that mode in its stability region (α_i >0), as in Fig. 4, a detour in the complex y-plane has to be done. In addition the detour cannot be arbitrary and is chosen so that the solution to the inviscid problem following that contour is the same as the solution to the viscous problem. While this analytical construction can be done in the EVP, it is more difficult to achieve in the LEE solver where y has to be real. However, the next section shows that using selective filtering in the LEE plays a similar role to using a complex mapping in the EVP.

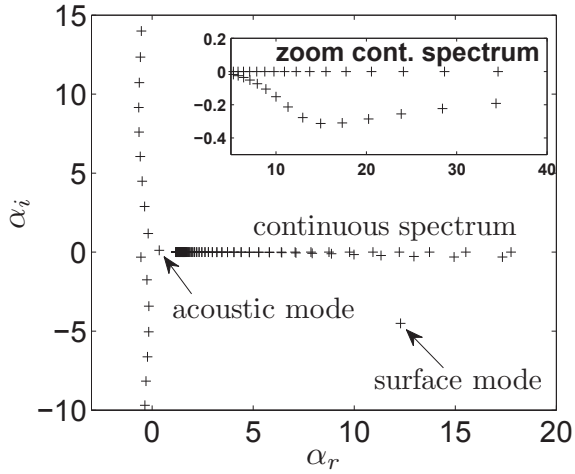

Figure 3 – Spectrum for R=1.2, σ=0, ω ~0.47.

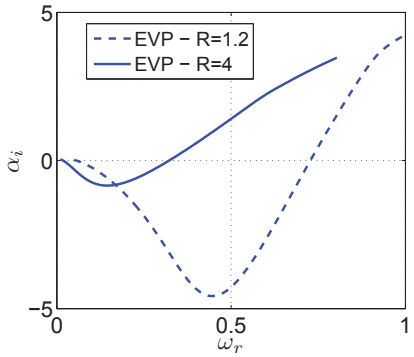

Figure 4 – Evolution of α_i (the opposite of the spatial growth rate) with real ω_r, for two different values of R.

5.2 Continuous spectrum and selective filtering

In addition to the surface mode, the continuous spectrum is seen in Fig. 3. This should lie along the real axis, but a bulge is observed which is located in the bottom plane, indicating that the continuous spectrum is made of spurious instabilities (the modes have α_i <0 and propagate in the x > 0 direction). This bulge is apparently related to a surface mode nearby, be it stable or unstable, and would not be seen for a rigid wall. In the present case with ω=0.47 the flow is unstable and the physical instability has a much larger growth rate than the spurious components of the discrete spectrum. However, for some frequencies, the flow may be stable while the continuous spectrum is unstable, as it is the case in Fig. 5 for ω=0.8. One characterictics of the "modes" of the continuous spectrum is that they have a discontinuous axial velocity at the critical layer. And one expects suppressing these modes by using a low pass filter that damps these modes. A selective filter is precisely used in the LEE and the effect of the selective filter (in the

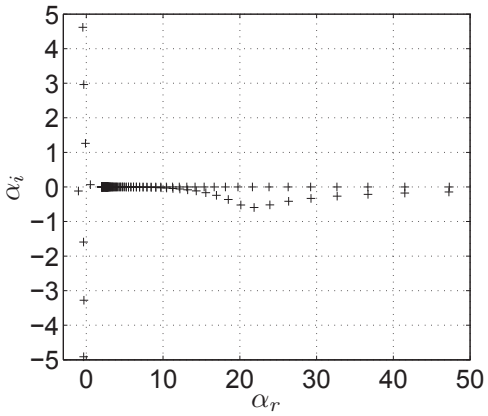

FIGURE 5 – Spectrum for R=1.2, σ=0, ω ~0.8. Chebyshev N=200. Without selective damping.

y-direction only) may be accounted for in the EVP as well. The effect on the spectrum at ω=0.8 is seen in Fig. 6 where the magnitude of the filter corresponds to a realistic LEE solution. Compared to the spectrum without damping, the continuous spectrum has been shifted to the α_i >0 plane, meaning that the modes are not unstable anymore. It should be said that this shift is not systematic and has more chance to be effective with a high resolution method (A Chebyshev method with many points will shift the continuous spectrum, while a DRP scheme with fewer points may leave some modes of the continuous spectrum in the bottom α-plane). An alternative view of the effect of selective filtering is

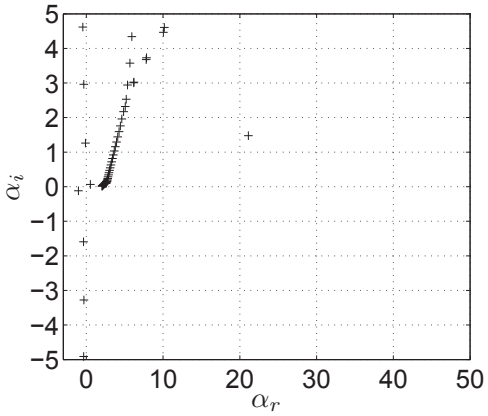

FIGURE 6 – Spectrum for R=1.2, σ=0, ω ~0.8. Chebyshev N=200. With selective damping.

seen when tracking the surface mode wavenumber while changing $\omega \in R$, as shown in Fig. 7. The correct result is for the complex contour y (dotted line, this is the same result as in Fig. 4). For a real $y \in$ (-1,1) and no damping (dashed line), the mode is correctly described whenever it is unstable and then get lost amidst the continuous spectrum for ω_r >0.65. The dashed line for ω_r >0.65 is actually made of modes of the continuous spectrum. When solving numerically the LEE it is not possible to work in the complex y-plane as for the EVP. But the result obtained with a real y and the selective filtering (plain line) actually approaches the result obtained with a complex map. The reason is that the selective filter shift the continuous spectrum in the upper α-plane, thus leaving some room for the surface mode to be tracked correctly. Of course, the effect of the selective filtering is to add some dissipation, which regularizes the inviscid problem, and the complex map (or physical viscosity) acts in the same way. The conclusion here is that for a sufficiently fine discretization the selective filtering removes the spurious continuous spectrum, leaving just the physical instability.

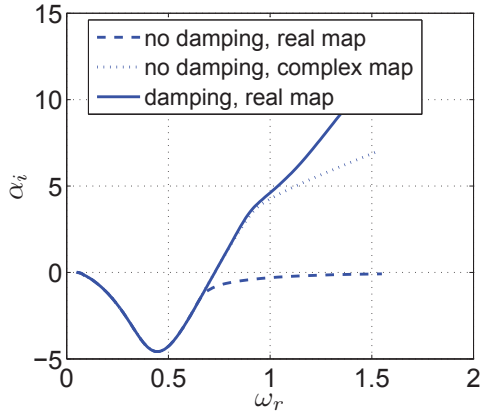

FIGURE 7 – Tracking of the surface mode wavenumber imaginary part (inverse of the growth rate) when varying real ω. R=1.2, σ=0. Chebyshev N=200.

5.3 Physical instability

The flow is now computed using the LEE in order to see whether the physical unstable mode predicted by solving the EVP can be observed numerically. To trigger an instability, it is necessary to introduce some kind of perturbation into the flow. This could be achieved by emitting a pulse above the material. Alternatively, we introduce at the input of the computational domain an acoustic wave of given frequency ω=0.47. If the medium does not contain initially any perturbation, switching on the acoustic wave is sufficient to introduce the desired perturbation. Even if the acoustic mode is used to set up an initial field within the computational domain (including auxiliary variables), an instability develops due to numerical noise, filtering, or imperfect sponge layers.

For R=1.2, an instantaneous pressure field is shown in Fig. 8. A short wavelength surface instability develops

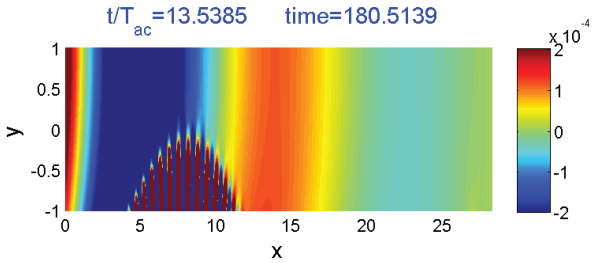

FIGURE 8 – Pressure snapshot. N_x=950, N_y=200.

against the large wavelength acoustic field. As time passes by, the wavepacket move toward x >0 while growing in amplitude. Ultimately it reaches a huge amplitude and even a small reflection of this by the output sponge layer ends up affecting the input sponge layer. The evolution of the logarithm of the pressure modulus with x is shown at a later time in Fig. 9. Upstream of the wave front, the envelope of

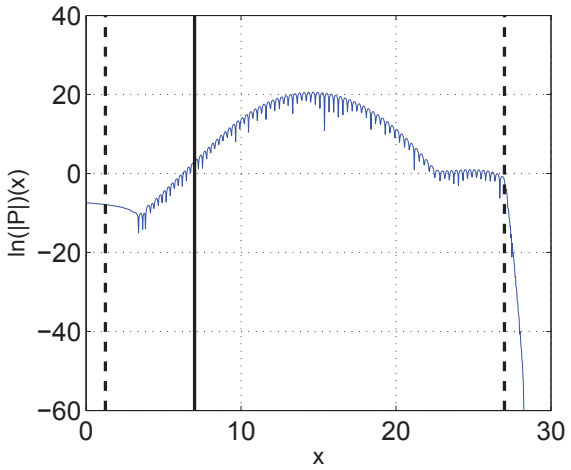

FIGURE 9 – ln(|$p(x)$|) vs x. R=1.2. t/T_{ac} ~27.

this evolution is linear and indicates an exponential spatial growth. By considering consecutive streamwise positions over a wavelength (the position is shown by a vertical thick line in Fig. 9), it is possible to extract the wavenumber and the eigenfunction of the observed instability. The time evolution at the same spatial positions provides the frequency of the wave. This information can be compared with the EVP result. Comparison for several cases is shown in Table 1. In this table, ω_{max} is the frequency for maximal

TABLE 1 – Characteristics of the instability wave.

Config	EVP		LEE	
	ω_{max}	α_{max}	ω_{max}	α_{max}
R=1.2, N_y=200	0.46	11.3-3.96i	0.47	12.4-4.06i
R=1.2, N_y = 100	0.43		0.45	11.2-3.3i
R=4, N_y=200	0.15	4.9-0.87	0.16	5.37-0.885i

spatial growth rate, and α_{max} is the corresponding wave number. For R=1.2, the frequency for maximal spatial amplification is about 0.47, which also corresponds to the frequency of the injected acoustic wave. The frequency observed in the LEE corresponds to this value. For R=4, the frequency for maximal spatial amplification given by the EVP is about 0.15, and it is not too far from the observed frequency with the LEE. In that case, the natural frequency is observed despite the input acoustic forcing is at ω=0.47. As said before, the input is probably imperfect in some sense so that it excites many frequencies, not just the forcing one, and only the most amplified frequency emerges from all the waves.

The eigenfunction modulus and phase of the axial velocity $\hat{u}$ are compared in Figs. 10-11. It is seen that the agreement is very good. It is clear that the instability observed in the LEE is physical and can be predicted by solving the EVP.

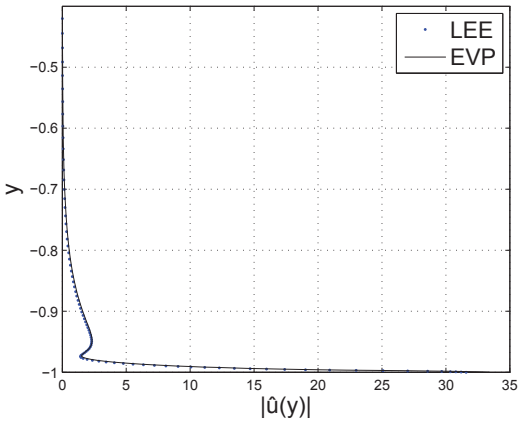

FIGURE 10 – Modulus of the eigenfunction. R=1.2, N_y=200.

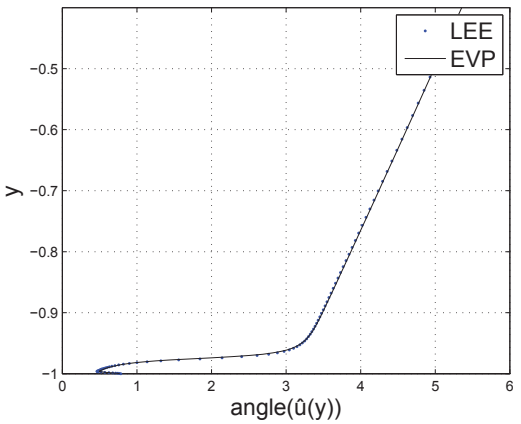

FIGURE 11 – Phase of the eigenfunction. R=1.2, N_y=200.

5.4 Rigid/Lined transition

The bottom wall is now made of three sections : a rigid one, a lined section, and finally a rigid section again. The same geometry as in Jones *et al.* [4] is considered. The quasi-plane mode (solution of the EVP) is introduced through the left sponge layer with frequency ω=0.47, and the liner is the same as previously with R=4 (chosen because the growth rate remains moderate in this case). Note that while the geometry and flow are similar to that of Jones *et al.* the lining properties have been chosen more arbitrarily (the liner is unstable with maximal growth rate at ω ~0.16). Several pressure snapshots are presented in Fig. 12. At the first instant considered (Fig. 12(a)), an unstable wavepacket has already formed at and detached from the leading edge of the liner and is travelling downstream. The frequency content of this wave packet corresponds to the unstable surface waves predicted by the EVP. In Fig. 12(b) this wave packet impinges the trailing edge of the liner and this produces high amplitude acoustic waves upstream and downstream. A a later time, Fig. 12(c), the intense acoustic radiation created by the wave packet crossing the liner/rigid transition is still present. The wave packet which has crossed the limit of the lined region through the right boundary propagates downstream along the rigid boundary while being damped (it is assumed that this wave packet is formed of modes of the continuous spectrum of the rigid wall but this has not been investigated). A new wave packet appears at the leading edge of the liner. This wave packet has its amplitude growing while moving downstream, as seen in Fig. 12(d), and this amplitude

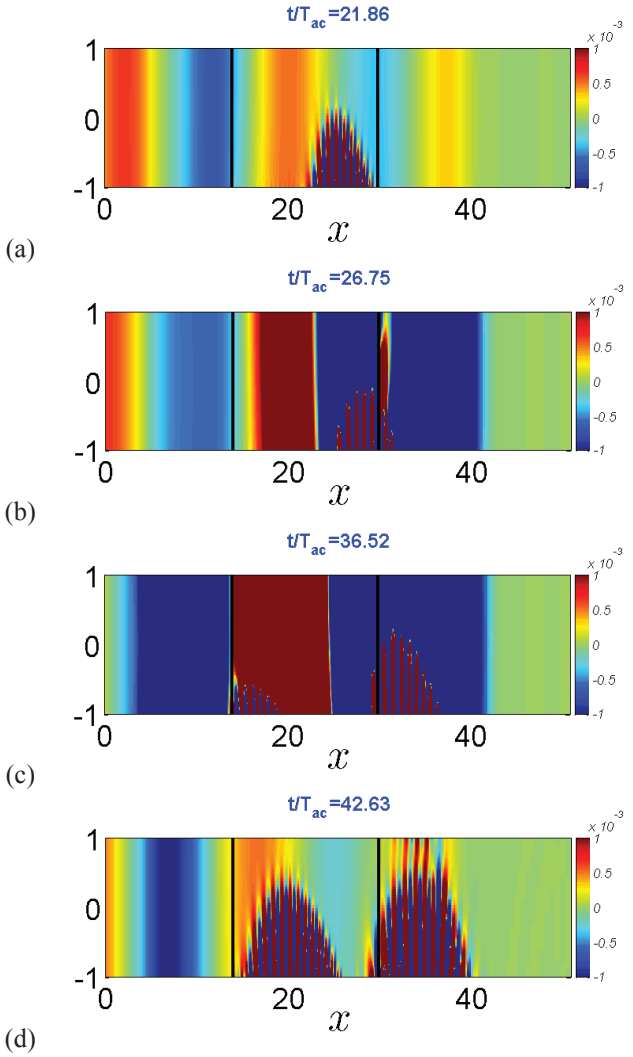

FIGURE 12 – Snapshots of the pressure at several instants. Rigid/lined/rigid bottom wall. R=4. The rigid/liner transition and the liner/rigid transition are indicated by a vertical line.

is more important that the one of the first wave packet amplitude seen in Fig. 12(a). When this new wave packet impinges the trailing edge of the liner, it produces a new acoustic wave of large amplitude (not shown). The injected acoustic mode has not been turned off but it seems that the process can sustain itself without this mode, meaning that the flow becomes absolutely unstable following a pressure feedback due to reflections at lined/rigid transitions (the liner is only convectively unstable). Of course this needs to be investigated further. It is likely that the mesh refinement at the rigid wall / liner transition plays an important role. Also, as the acoustic waves travelling from the liner to the exit of the computational domain have an increasing amplitude, it is important to have a very good non-reflecting boundary condition.

6 Conclusion

The propagation in a lined channel has been computed numerically using the LEE in the presence of a mean velocity profile having a large shear and null velocity at the walls. The liner model at the bottom wall is a Mass-Spring-Damper system and the impedance is imposed without using the Myers boundary condition. A physical instability has been observed whose characteristics can be predicted by solving a matrix EVP. The role of the numerical selective filtering in removing the spuriously unstable continuous spectrum has been discussed. It has also been shown that unstable modes above liners create strong acoustic modes at rigid wall / liner transitions.

Références

[1] Richter, C., Hay, J., Panek, L., Schonwald, N., Busse, S., Thiele, F., A review of time-domain impedance modelling and applications, *Journal of Sound and Vibration* **330**, 3859–3873 (2011).

[2] Tam, C. K. W., and Auriault, L., Time-Domain Impedance Boundary Conditions for Computational Aeroacoustics, *AIAA Journal* **34** 917-923 (1996).

[3] Li, X., Richter, C., Thiele, F., Time-domain impedance boundary conditions for surfaces with subsonic mean flows,*Journal of the Acoustical Society of America*, **119** 2665–2676 (2006).

[4] Jones, M. G.,Watson, W.R., Parrott, T.L., Benchmark data for evaluation of aeroacoustic propagation codes with grazing flow, *11th AIAA/CEAS Aeroacoustics Conference*, AIAA Paper 2005-2853 (2005).

[5] Ozyoruk, Y., Long, L. N., Time-domain calculation of sound propagation in lined ducts with sheared flows, *AIAA Journal* **39** 768–773 (2000).

[6] Zheng, S., Zhuang, M., Verification and validation of time-domain impedance boundary condition in lined ducts, *AIAA Journal* **43** 306–313 (2005).

[7] Ozyoruk, Y., Long, L. N., Jones, M. G., Time-domain numerical simulation of a flow-impedance tube, *J. Comput. Phys.* **146** 29–57 (1988).

[8] Brambley, E. J., "Fundamental problems with the model of uniform flow over acoustic linings," *Journal of Sound and Vibration* **322** 1026–1037 (2009).

[9] Marx, D., A piecewise linear mean flow model for studying stability in a lined channel, *Journal of Sound and Vibration* **331** 3809–3823 (2012).

[10] Richards, S.K., Zhang, X. , Chen, X.X., Nelson, P.A., The evaluation of non-reflecting boundary conditions for duct acoustic computation, *Journal of Sound and Vibration* **270** 539–557 (2004).

[11] Bogey, C., and Bailly, C., A Family of Low Dispersive and Low Dissipative Explicit Schemes for Flow and Noise Computations, *Journal of Computational Physics* **194** 194–214 (2004).

[12] Marx, D., Aurégan, Y., Effect of turbulent eddy viscosity on the unstable surface mode above an acoustic liner, *J. Sound Vib.* **332** 3803–3820 (2013).

[13] Shankar, P. N., Sound propagation in duct shear layers, *Journal of Sound and Vibration* **22** 221-232 (1972).